

# Planar digital nanoliter dispensing system based on thermocapillary actuation

Anton A. Darhuber,<sup>\*a</sup> Joseph P. Valentino<sup>b</sup> and Sandra M. Troian<sup>c</sup>

Received 19th October 2009, Accepted 16th December 2009

First published as an Advance Article on the web 3rd February 2010

DOI: 10.1039/b921759b

We provide guidelines for the design and operation of a planar digital nanodispensing system based on thermocapillary actuation. Thin metallic microheaters embedded within a chemically patterned glass substrate are electronically activated to generate and control 2D surface temperature distributions which either arrest or trigger liquid flow and droplet formation on demand. This flow control is a consequence of the variation of a liquid's surface tension with temperature, which is used to draw liquid toward cooler regions of the supporting substrate. A liquid sample consisting of several microliters is placed on a flat rectangular supply cell defined by chemical patterning. Thermocapillary switches are then activated to extract a slender fluid filament from the cell and to divide the filament into an array of droplets whose position and volume are digitally controlled. Experimental results for the power required to extract a filament and to divide it into two or more droplets as a function of geometric and operating parameters are in excellent agreement with hydrodynamic simulations. The capability to dispense ultralow volumes onto a 2D substrate extends the functionality of microfluidic devices based on thermocapillary actuation previously shown effective in routing and mixing nanoliter liquid samples on glass or silicon substrates.

## I. Introduction

Automated liquid handling systems are rapidly replacing conventional pipetting technologies in many biological and pharmaceutical applications. Integrated microfluidic networks which combine transport, mixing and reaction assays on a single miniature platform are becoming more commonplace, since these devices offer highly parallel and automated processing of very low liquid volumes, thereby minimizing contamination and cost. Depending on the fluid sample characteristics and application at hand, various methods for transporting liquid films and droplets have been developed during the past decade.<sup>1</sup> The majority of methods rely on internal flow in enclosed microchannels induced, for instance, by pressure gradients,<sup>2</sup> electroosmosis<sup>3</sup> or thermocapillary pumping.<sup>4</sup> Alternative methods employ mechanisms for transport and mixing along the exterior surface of materials such as glass or silicon. These methods modulate so-called surface-directed or free-surface flows, whereby forces exerted perpendicular or parallel to a gas-liquid or liquid-liquid interface are utilized to propel liquid samples along substrate pathways. These techniques offer flow control without moving parts and facilitate integration of optical interrogation and detection schemes, since the surface of the liquid is fully exposed. Methods within this category include electro-wetting,<sup>5,6</sup> dielectrophoresis,<sup>7,8</sup> surface-acoustic waves<sup>9</sup> and thermocapillary propulsion.<sup>10</sup> With each of these techniques, discrete droplets can be transported along a planar substrate by activation of embedded electrodes or microheaters.

In this work we focus on a critical step in automated fluid handling – the dispensing and metering of small liquid sample volumes onto “lab-on-a-chip” devices. There have been a number of methods proposed for introducing liquid samples to a diagnostic platform with or without contacting the target surface.<sup>11</sup> Non-contact techniques often use air- or liquid-based ejection techniques (*i.e.* positive-displacement techniques) to dispense droplets from slender capillaries onto a substrate target. Ejection volumes are not always reproducible to the degree desired, especially for very viscous liquids or volumes below a microliter. Rapid delivery is enhanced through piezoelectric actuation,<sup>12–14</sup> as implemented in commercial ink jetting systems. Ultra small liquid quantities can be delivered by contact methods such as pin transfer or stencil printing methods, as used industrially for deposition of solder or adhesives to printed circuit boards. Solid or slotted pins are used to transfer precise volumes of liquid by capillary detachment from a metal or glass tip onto a dry surface. These methods are especially suited to volumes in the sub 100 nL range. The pins do not need to be disposed of after single use, however, extensive washing and blotting are necessary to prevent cross contamination of samples. More recently, such contact methods have been extended to spotting of DNA microarrays<sup>15,16</sup> and the utilization of AFM tips for transfer of volumes in the attoliter range.<sup>17–20</sup>

From the perspective of microfluidic integration, it would be ideal if all fluidic processes, such as dispensing, routing, mixing, activation and quenching of chemical reactions, could be implemented by utilizing a single tunable external mechanism. It has been demonstrated, for example, that ionic or electrolytic solutions can be mobilized and dispensed along a surface by the technique known as electrowetting. Cho *et al.*<sup>21</sup> and Pollack *et al.*<sup>22</sup> have used this method to extract a slender liquid filament from a larger reservoir onto a linear electrode array. Activation of selected electrodes near the tip of the filament causes the liquid

<sup>a</sup>Mesosopic Transport Phenomena Group, Department of Applied Physics, Eindhoven University of Technology, Den Dolech 2, 5612AZ Eindhoven, The Netherlands. E-mail: a.a.darhuber@tue.nl

<sup>b</sup>Fish & Richardson P.C., NY, NY

<sup>c</sup>California Institute of Technology, 1200 E. California Blvd, Dept. of Applied Physics, MC 128-95 Pasadena, CA. E-mail: stroian@caltech.edu

thread to split into smaller droplets ranging in volume from 50–100 nL. Ren *et al.*<sup>23</sup> implemented a capacitive technique for measuring the volume of droplets dispensed in this way as a function of droplet formation rate, fluid viscosity and channel aspect ratio. Reproducibility of droplet volumes ranged from about 1–9% but was further reduced for lower rates of droplet formation or with liquids of lower viscosity. Yi *et al.*<sup>24</sup> employed a similar dispensing technique for transferring water droplets or DNA solutions onto the surface of a glass substrate. A review of fundamental aspects and applications of electrowetting can be found in ref. [25].

In a similar fashion, dielectrophoretic forces have been used to dispense small volumes of liquid ranging from 5–100 nL using coplanar, bisected circular electrodes.<sup>8</sup> Even smaller droplet volumes in the range of 4–500 pL have been generated using dielectrophoretic based injection through glass capillaries with an internal diameter ranging from 2–4  $\mu\text{m}$ .<sup>26</sup> In a process akin to dip-coating of chemically patterned striped substrates,<sup>27</sup> Strobl *et al.*<sup>9</sup> used a surface acoustic wave technique for transporting a larger water droplet over a substrate patterned into hydrophilic dots with hydrophobic surroundings. Migration of the drop along the hydrophilic array caused detachment of drops in the pL range adhering to the hydrophilic areas.

Droplet formation due to capillary break-up of liquid filaments or bridges is regarded as a *passive* process since droplet detachment occurs through a Rayleigh-like instability of the liquid thread.<sup>28–30</sup> The reproducibility of dispensing mechanisms based on capillary instabilities can be problematic for certain applications, however, since it is challenging to achieve precise control over the exact location of breakup points.

Alternative techniques exist where modulation of interfacial stresses induces fluid transport and break-up. In previous work, we have examined thermocapillary actuation of liquid films, droplets and filaments on chemically patterned surfaces.<sup>1,10,31–34</sup> Darhuber *et al.* deposited a large droplet on an open, chemically defined supply cell and investigated the spreading behavior of liquid filaments extracted onto completely wettable microstrips either by *passive* means such as spontaneous capillary driven spreading<sup>31</sup> or active means such as thermocapillary triggered flow.<sup>33</sup> In the latter study, an array of embedded thin film microheaters was used to generate 1D thermal gradients such that a liquid ribbon was made to flow from warmer to cooler regions of a glass substrate. In separate studies, similar digital control was used to develop a microfluidic device capable of mobilizing discrete droplets along more complex trajectories of a microfluidic chip.<sup>10,32</sup> A multitude of surface pathways for droplet routing were defined by chemically patterning the glass surface into wettable stripes against a non-wetting background. The actual droplet trajectories were then controlled by activation of selected microheaters embedded beneath the wettable stripes. These devices were further expanded to include both capacitive<sup>34</sup> and evanescent wave sensing,<sup>35</sup> useful for automated control of droplet position as well as local interrogation of droplet composition. Thermocapillary actuation has also been used to induce and control mixing in flowing co-current microstreams made to coalesce within an open (*i.e.* exposed) Y-junction.<sup>36</sup> Other groups have been investigating the use of thermocapillary control enforced by microheater arrays situated above the liquid or remote heating from a laser source. Kotz *et al.* has used

near-infrared laser irradiation to propel water droplets immersed in decanol for the purpose of protein assays.<sup>37</sup> Baroud *et al.* have used laser-induced modulation of the interfacial tension of an oil-water interface to dispense and steer droplets flowing in an enclosed microchannel.<sup>38</sup> Basu and Gianchandani<sup>39</sup> have explored thermocapillary actuation of droplets floating on an immiscible mineral oil film by means of overhead heating elements, thus demonstrating *virtual* microfluidic traps, filters, channels and pumps. Yap *et al.* has utilized microheaters to control the volume and trajectories of water droplets suspended in mineral oil at a T-junction of enclosed microchannels.<sup>40</sup>

In what follows, we provide guidelines for the design and operation of a planar digital nanodispensing system based on thermocapillary actuation. Thin film microheaters embedded within a chemically patterned glass substrate are digitally activated to produce 2D surface temperature distributions which either arrest or trigger liquid flow and droplet scission on demand. Several microliters of liquid samples are first placed on the surface of planar wetting supply cells defined by chemical patterning. Thermocapillary switches are then activated to extract a liquid thread from this reservoir onto a wettable strip and to induce splitting of the thread into one or more nanoliter droplets, whose position and volume is electronically controlled. Experimental results for the power required to extract a filament of specified length and to divide the filament into two or more droplets as a function of geometric and operating parameters are in excellent agreement with hydrodynamic simulations. The parameter range explored in simulations is extended beyond the design of the current device in order to provide useful scaling relationships for future device development.

## II. Experimental setup

The microfluidic device designed for this study combines temperature-gradient-driven flow<sup>1</sup> with chemical surface patterning to guide the formation of liquid films, filaments and droplets. In response to thermal modulation of the surface tension  $\gamma(T_s)$ , liquid elements flow toward cooler regions of the substrate surface temperature distribution  $T_s(x, y)$ . An array of embedded metallic microheaters allows variation and adjustment of the surface temperature which in turn directs the location and configuration of the liquid. The chemical patterning is achieved by dividing the substrate surface into wetting and non-wetting regions<sup>41</sup> defining a rectangular supply cell and striped pathways emanating from there. For the fluids and volumes investigated in this study, the liquid was always confined to the wettable regions enclosed by the dashed lines shown in Fig. 1(a).

### A. Device fabrication

As sketched in Fig. 1(a) and (b), the devices were fabricated on Corning 1737F glass substrates of thickness  $d_{\text{sub}} = 0.7$  mm and thermal conductivity  $k_{\text{sub}} = 1.0$  W/m · K. A periodic array of Ti microheaters of length  $l_R = 3$  mm, width  $w_R = 0.8$  mm and thickness 100 nm was evaporated onto the glass substrate and then coated with a 500 nm layer of vapor deposited  $\text{SiO}_2$  for electrical insulation.<sup>32</sup> The chemical surface patterning was achieved by selectively applying a self-assembled monolayer of 1H,1H,2H,2H-perfluorooctyl-trichlorosilane (PFOTS, Aldrich)

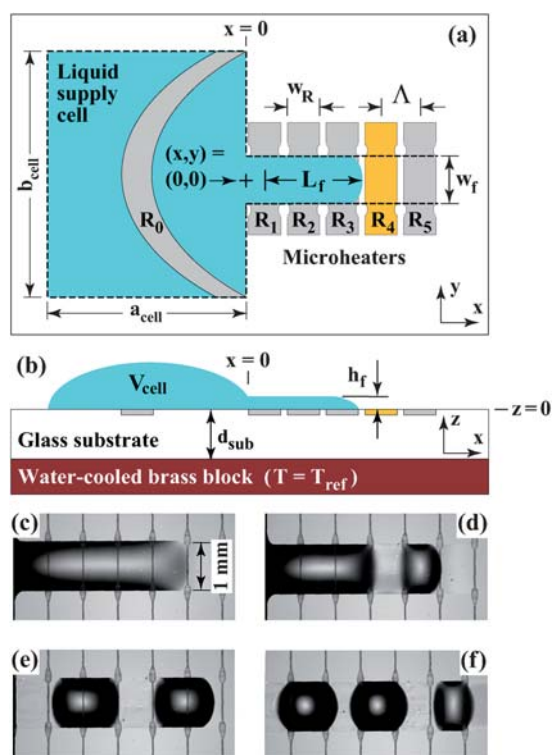


**Fig. 1** Top (a) and cross-sectional (b) views of microfluidic device fabricated on a glass substrate. The area enclosed by dashed lines signify regions of the substrate which are completely wetting and consist of a planar supply cell of area  $a_{\text{cell}} \times b_{\text{cell}} = 5.8 \times 7 \text{ mm}^2$  and a stripe of width  $w_f = 0.5\text{--}2 \text{ mm}$ . The filament length,  $L_f$ , is measured from the leading edge of the liquid to the center of the resistor used for splitting, which was usually  $R_1$ . (c) Optical micrograph of a 1 mm wide liquid filament separated electronically into (d) one, (e) two and (f) three droplets.

to the  $\text{SiO}_2$  layer. For this purpose, the sample was immersed in a 1 mM solution of PFOTS in dodecane for 10 min at room temperature after masking the wettable regions by means of photolithography. The areas not coated by this monolayer remained completely wetting.

The microheater array period was chosen to be  $\Lambda = 860 \mu\text{m}$ . The left edge of  $R_1$  was aligned with the rightmost edge of the supply cell defined in Fig. 1(a) as  $x = 0$ . The ratio of the microheater width,  $w_R$ , to the width of the liquid filament,  $w_f$ , is an important design parameter, as will be shown. The smaller this ratio, the higher the spatial resolution with which the surface temperature can be adjusted. The larger this ratio, the fewer microheaters are needed for given device dimensions. For the devices fabricated for this study,  $w_R/w_f \approx 1$ . In order to define a constant reference temperature for operation and implementation of surface temperature gradients, the glass substrate was affixed to a water cooled brass block maintained at room temperature by means of a  $10\text{--}50 \mu\text{m}$  thick layer of heat-transfer paste (Sunhayato SCH-20, thermal conductivity  $0.84 \text{ W/m} \cdot \text{K}$ ).

The device was always operated in a horizontal orientation; the device was placed on a vibration-isolated table situated within a HEPA-filtered laminar flow hood that delivered a gentle horizontal air stream to minimize dust and contamination within the measurement area. Optical micrographs were recorded using

a Zeiss Axiotech Vario microscope equipped with a DVC CCD camera and an optical filter with a bandpass centered at 650 nm.

## B. Electronic microheater control

The electrical resistance  $R_i$  of the Ti microheaters was measured to be  $123 \Omega$ . The resistance of resistor  $R_0$  embedded beneath the supply cell shown in Fig. 1(a) was measured to be  $400 \Omega$ . The surface area comprising  $R_0$  corresponded to the area in between two identical arcs of a circle of 4 mm radius displaced from each by a distance  $800 \mu\text{m}$  along the  $x$ -axis. The shape of all other microheaters was chosen to be rectangular with 4 shallow constrictions located symmetrically at  $y \approx \pm 600 \mu\text{m}$  for the purpose of creating a shallow temperature minimum in the middle of the wetting stripe. This small adjustment helps optimize the liquid flow profile as explained in ref. [32].

The electronic control used for addressing the individual microheaters comprised two 32-channel digital-to-analog (D/A) boards, a 96-channel digital input/output board and two custom-made printed circuit boards (PCBs) with MOSFET switches and flip-flops. The microheaters were connected to the PCBs by means of two 50-pin card-edge-connectors with a contact spacing of 2.54 mm. All electronic components were controlled by Lab-View 6.0 software.<sup>32</sup> The power applied to individual microheaters,  $P_i = V_i^2/R_i$ , typically ranged from 5–200 mW, and was estimated from the nominal output voltages,  $V_i$ , from the D/A boards (maximum output voltage 10 V, max. output current 90 mA) after correcting for parasitic and lead resistances. Changes in the microheater resistance  $\Delta R_i$  due to temperature increases  $\Delta T$  could be neglected<sup>42–44</sup> since  $\Delta R_i/(R_i \Delta T)$  was estimated at approximately  $0.001 \text{ K}^{-1}$ .

## C. Device operation

To initiate the dispensing process, a liquid reservoir volume of  $V_{\text{cell}} = 3\text{--}16 \mu\text{l}$  was first deposited onto the planar supply cell shown in Fig. 1(a) by means of a Hamilton glass syringe (25 nl resolution). Liquid in the supply cell, measuring 5.8 mm by 7 mm, flowed onto a wettable planar stripe of width  $w_f = 0.5\text{--}2 \text{ mm}$  situated directly above the microheater array. The liquid flowed spontaneously onto the stripe either by capillary and hydrostatic action or thermal assist from resistor  $R_0$  for faster dispensing. The volume exiting the reservoir was controlled by activating a selected microheater, which would cause a local reverse thermocapillary flow to arrest spreading of the liquid filament. In the example shown in Fig. 1(c), activation of microheater  $R_4$  [colored orange (online) in Fig. 1(a,b)] stopped the flow of liquid to the location defined by the left edge of the heater. Subsequently, other microheaters were activated to induce scission and droplet formation at one or more locations as shown in Figs. 1(d–f)]. In addition to specification of the original filament length, the timing of the dispensing process as well as the volume and location of nanodroplets formed can be continuously and electronically controlled. Once a given array of droplets is formed, additional microheater arrays arranged either parallel or perpendicular to the stripe shown can be activated to transport droplets across the surface of the device for further mixing or analysis. Use of just a single tuning parameter, namely

the substrate surface temperature field, therefore provides a simple and robust means of transport with no moving parts.

#### D. Liquid material properties

The liquid chosen for this study was polydimethylsiloxane silicone oil DC200 (PDMS from Fluka), a non-volatile liquid<sup>46</sup> which was found to be completely wetting on portions of the glass substrate not treated with the PFOTS monolayer but repelled from the treated areas. Additional material properties relevant to this study are the liquid surface tension,  $\gamma = 20.0$  mN/m, and its variation with temperature,<sup>45</sup>  $\partial\gamma/\partial T = -6.0 \times 10^{-5}$  mN/(m · K), viscosity  $\mu = 18$  mPa · s and density  $\rho = 954$  kg/m<sup>3</sup>.

### III. Fluid dynamical analysis

The flow of liquid in the system shown in Figs. 1(a) and (b) is due to thermocapillary shear stresses induced by substrate temperature gradients as well as gradients in capillary and hydrostatic pressure due to variations in liquid film height and surface curvature induced by the specific geometry of the areas outlined by dashed lines. For completely wetting liquids and even in the absence of thermocapillary stresses, flow will occur spontaneously from the reservoir onto a stripe.<sup>31</sup> Activation of the microheaters generates non-uniform surface temperature profiles  $T_s(x, y)$  which can be used to modulate the liquid surface tension  $\gamma[T_s]$  in space and time, thereby providing a dominant and electronically controlled force for transport. In addition, the resulting thermocapillary force per unit liquid surface area  $\tau \rightarrow = \nabla_{\parallel}\gamma = (\partial\gamma/\partial T)\nabla_{\parallel}T_s$  can be utilized for a variety of tasks: (1) to counteract capillary and gravitationally induced spreading, (2) to thicken or thin liquid filaments at specified locations, (3) to form discrete droplets at desired positions, and (4) to propel droplets or films along wettable stripes. The vector operator  $\nabla_{\parallel}$  designates the surface gradient  $\nabla_{\parallel} = \nabla - \hat{n}\hat{n} \cdot \nabla$ , where  $\hat{n}$  denotes an outwardly pointing unit normal vector. Within the lubrication approximation, the surface gradient operator becomes  $(\partial/\partial x, \partial/\partial y)$ .

In the next section, the results of numerical model calculations are presented in order to obtain reliable estimates for the droplet volumes dispensed as well as the power requirements necessary to each process step. Essential to these computations is accurate determination of the substrate surface temperature  $T_s(x, y) = T(x, y, z = 0)$  needed for assessment of the local thermocapillary stress.

#### A. Heat transfer calculations

Under typical operating conditions, heat losses to the ambient air were determined to be negligible in comparison to the heat flux generated by the microheaters. Thermal convection effects could also be ignored since the ratio of liquid thickness to lateral span as well as the fluid speed were sufficiently small such that the Biot and thermal Peclet numbers were both of order  $10^{-3}$ . These operating limits leads to two important consequences. There develops essentially no vertical gradient in temperature within the liquid since the local temperature of the substrate in the absence of liquid is essentially equal to the local temperature of the air/liquid interface with liquid present. This then leads to a decoupling of the equations describing the heat transfer and fluid flow. The substrate surface temperature distribution  $T_s(x, y)$

computed from a 2D conduction problem can then be input into the thermocapillary stress term necessary to the hydrodynamic simulations.

The thermal distribution  $T_s(x, y)$  in the absence of liquid was obtained from solution of the steady-state heat conduction equation  $\nabla^2 T = 0$  throughout the solid portions shown in Fig. 1(b) and Figs. 2(a,b). This equation was solved by finite element simulations using triangular or tetrahedral elements with quadratic basis functions. The boundary conditions (BCs) corresponding, for example, to activation of microheater  $R_1$  are shown in Fig. 2 and given by:

- Bottom surface ( $z = -d_{\text{sub}}$ ): Perfect thermal contact with a water-cooled brass block

$$T(x, y, z = -d_{\text{sub}}) = 293 \text{ K} \quad (1)$$

- Top surface ( $z = 0$ ): Localized heat flux provided by activation of individual microheater

$$k_{\text{sub}} \frac{\partial T}{\partial z}(x, y, z = 0) = \dot{q}(x, y) \quad (2)$$

where  $\dot{q}(x, y)$  represents the Joule heat flux caused by the electrical current flowing through the microheater where

$$\dot{q}(x, y) = \begin{cases} \frac{P_1}{w_R l_R} & |x| \leq w_R/2 \text{ and } |y| \leq l_R/2 \\ 0 & |x| > w_R/2 \text{ or } |y| > l_R/2 \end{cases} \quad (3)$$

Implementation of this constant boundary heat flux from the microheater into a domain of homogeneous thermal

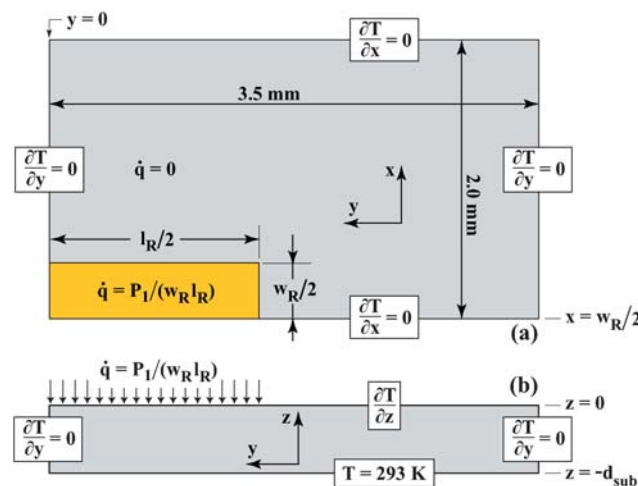


**Fig. 2** (a) Top-view and (b) side-view sketches of the computational domain and corresponding BCs used for solution of the 3D conduction problem. The small rectangle of dimensions  $\frac{w_R}{2} \times \frac{l_R}{2}$  represents one quarter of the microheater  $R_1$ . The BCs in the planes  $x = w_R/2 = 0.4$  mm,  $x = 2.4$  mm,  $y = 0$  and  $y = 3.5$  mm correspond to vanishing normal heat flux  $\mathbf{n} \cdot \nabla T = 0$ , where  $\mathbf{n}$  denotes an outwardly-oriented unit normal vector. The isothermal BC  $T = 293$  K imposed at the substrate bottom  $z = -d_{\text{sub}} = -0.7$  mm represents ideal thermal contact with a water-cooled brass block. Activation of a microheater is modeled by a position-dependent heat flux  $\dot{q}(x, y)$  distributed along the top surface,  $z = 0$ , where  $\dot{q} = P_1/(w_R l_R)$  within the rectangle (shown yellow in online version) and zero everywhere else.

conductivity is equivalent to neglecting the heat transfer through the microheaters and the SiO<sub>2</sub> capping layer due to their negligible thickness in comparison to the thickness of the glass substrate.

- Mirror planes ( $y = 0$  and  $x = w_R/2$ ): Vanishing heat flux normal to planes of mirror symmetry

$$\frac{\partial T}{\partial x}\left(x = \frac{w_R}{2}, y, z\right) = 0 \quad (4)$$

$$\frac{\partial T}{\partial y}(x, y = 0, z) = 0 \quad (5)$$

- Lateral domain boundaries ( $x = 2.4$  mm and  $y = 3.5$  mm): Vanishing heat flux at distances exceeding the thermal decay length for an activated microheater

$$\frac{\partial T}{\partial x}(x = 2.4 \text{ mm}, y, z) = 0 \quad (6)$$

$$\frac{\partial T}{\partial y}(x, y = 3.5 \text{ mm}, z) = 0 \quad (7)$$

The heat flux decays to zero several mm from the microheater center since the thermal decay length (discussed below) extends only approximately  $\xi \approx 0.9$  mm. The exact numerical values corresponding to 2.4 mm and 3.5 mm are therefore of no significance and chosen simply to mimic far field boundary conditions.

The lateral spread of the thermal profile in the  $x$ - and  $y$ -directions due to activation of a microheater is quantified by the decay length  $\xi$ . This length represents the distance away from a heater edge where the local increase in temperature diminishes to 10% of the value obtained at the microheater edge, *i.e.*

$$T_s\left(x_i + \frac{w_R}{2} + \xi, 0\right) - T_{\text{ref}} = \frac{1}{10} \times \left[T_s\left(x_i + \frac{w_R}{2}, 0\right) - T_{\text{ref}}\right]$$

Previous numerical simulations<sup>47</sup> indicate that the fall-off is well approximated by the relation  $\xi = 1.26 d_{\text{sub}} \approx 0.9$  mm, where in the present study  $x_i$  defines the center position of microheater  $R_i$ .

The finite length  $l_R$  of the microheaters was found to be important only for the (3D) heat transfer calculations for microheater  $R_1$  since the liquid on the supply cell is immediately adjacent to this heater. For resistors  $R_2$  and higher, accurate temperature distributions were obtained from a reduced 2D model corresponding to thermal conduction provided by infinitely long microheaters ( $l_R \rightarrow \infty$ ).<sup>47</sup> The microheater edges  $y = \pm l_R/2$  were sufficiently remote from both the filament and the supply cell such that temperature gradients in the  $y$ -direction could be ignored. The microheater indentations<sup>32</sup> shown in Fig. 1 were disregarded in the simulations in all cases.

Due the absence of convective and radiative cooling, the heat transfer process reduced to a linear equation describing thermal conduction through a glass substrate subject to a localized surface heat flux. Solutions can therefore be linearly superimposed to obtain the complete thermal profile. Moreover, increases in surface temperature and hence thermal gradients are simply proportional to the heater input power,  $P_i$ . The surface temperature distributions  $T(x, y, z = 0) = T_s(x, y)$  were therefore

computed only once for a power input of 100 mW (3D simulations for  $R_1$ ) or 100 mW/cm (2D simulations for  $R_2$  and higher) and then multiplied by a factor  $A_i = P_i/(100 \text{ mW})$  to account for different power settings. Similarly, when two microheaters were activated simultaneously, the total increase in surface temperature was obtained by linear superposition of the individual solutions, *e.g.*

$$T_s(x, y) - T_{\text{ref}} = A_1[T_{s, 1}(x, y) - T_{\text{ref}}] + A_4[T_{s, 4}(x, y) - T_{\text{ref}}]$$

Fig. 4(a) shows a typical temperature distribution. The surface temperature increase  $T_s - T_{\text{ref}}$  is highest in the center of an activated heater and amounts to approximately 2.2 K for an input power of 12 mW. The highest temperature gradients always occur at the microheater edges. For the time-dependent, hydrodynamic simulations described in the next section, thermal changes are assumed to occur instantaneously, since the convective time scale for fluid motion is orders of magnitude larger than the time scale associated with thermal conduction. The interested reader can find additional details pertaining to the heat transfer calculations in ref. [47] and [48].

## B. Fluidic calculations

The results of the surface temperature distribution  $T_s(x, y)$  can then be input into hydrodynamic simulations of the liquid flow under the action of thermocapillary stresses. Since the supply cell volumes  $V_{\text{cell}}$  used in this study were small, the corresponding aspect ratios were also small, namely  $(h_l/w_f)^2 \ll 1$  and  $(h_{\text{cell}}/w_{\text{cell}})^2 \ll 1$ . These geometric limits, coupled with the fact that the flow speeds are sufficiently small such that inertial effects can be ignored,<sup>49</sup> constitutes the so-called lubrication approximation, which greatly simplifies solution of the evolution equation<sup>50</sup> for the local liquid film thickness  $h(x, y, t)$ :

$$\frac{\partial h}{\partial t} + \frac{\partial Q_x}{\partial x} + \frac{\partial Q_y}{\partial y} = 0 \quad (8)$$

Here,  $(Q_x, Q_y)$  denotes the liquid flux vector along the  $x$  and  $y$  axes given by

$$Q_x = \frac{h^2 \tau_x}{2\mu} - \frac{h^3}{3\mu} \frac{\partial \mathcal{P}}{\partial x} = h\langle u \rangle \quad (9)$$

$$Q_y = \frac{h^2 \tau_y}{2\mu} - \frac{h^3}{3\mu} \frac{\partial \mathcal{P}}{\partial y} = h\langle v \rangle \quad (10)$$

where  $\langle u \rangle$  and  $\langle v \rangle$  represent the height-averaged flow speeds along the  $x$  and  $y$  axes and  $\tau_x = (\partial\gamma/\partial T) \partial T_s/\partial x$  and  $\tau_y = (\partial\gamma/\partial T) \partial T_s/\partial y$  represent the magnitude of the thermocapillary shear stress at the air/liquid interface  $z = h(x, y, t)$ . Within the lubrication approximation, the vertical pressure gradient vanishes and the augmented pressure  $\mathcal{P}$  within the film is equal to its value at the air-liquid interface  $z = h(x, y, t)$ , namely

$$\mathcal{P} = \rho gh - \gamma \left( \frac{\partial^2 h}{\partial x^2} + \frac{\partial^2 h}{\partial y^2} \right) \quad (11)$$

This augmented pressure represents the contributions of hydrostatic and capillary terms.

As shown previously for the case of long filaments  $L_f \gg w_f$  flowing under the influence of a *constant* temperature gradient,<sup>33</sup> Eq. (8) can be further reduced to a one-dimensional equation for the filament apex height  $h_c(x, t) = h(x, y = 0, t)$ . For the experiments conducted in the present study, however, the important longitudinal lengthscales  $L_f$ ,  $w_R$  and  $\xi$  are all fairly comparable in size to  $w_f$ . The two-dimensional nature of Eq. (8) was therefore retained in the computations and the system of equations solved accordingly.

**1. Numerical implementation and boundary conditions.** Eq. (8) was solved by finite element simulations using triangular elements with quadratic basis functions. The computational domain and corresponding BCs for fluid flow are shown in Fig. 3. For completely wetting fluids, the contact line  $h = 0$  coincides with the perimeter of the wettable regions defined by the dashed lines in Fig. 1(a). The BC along  $y = 0$  reflects the mirror-symmetry of the device layout.

The stripe length  $L$  was always chosen to be sufficiently long such that liquid filaments or droplets never reached the location  $x = L$  during a given simulation. The BCs at this location were specified to be  $\partial h/\partial x = 0$  and  $Q_x = 0$ .

Two additional approximations were implemented in this study. For the liquid used in the experiments, the relative change in surface tension with temperature  $\Delta\gamma/\gamma = (\partial\gamma/\partial T)(\Delta T/\gamma)$  ranged only from 0.003–0.075 for temperature changes  $\Delta T$  spanning 1–25 K. As a result, the temperature dependence of  $\gamma$  in the Laplace pressure in Eq. (11) could be ignored. The temperature dependence of the liquid viscosity  $\mu$  in Eq. (8) was also neglected despite that  $\Delta\mu/\mu \approx 0.017$ –0.36 for  $\Delta T = 1$ –25 K. Although the relative change in viscosity is not much less than unity, this approximation remains valid for the current study since the focus is on steady-state solutions wherein the viscosity dependence plays no role, since both terms in the expressions for  $Q_x$  and  $Q_y$  scale identically with  $\mu$ .

**2. Initial conditions.** In order to avoid the well known stress singularity at a moving triple contact line,<sup>51–54</sup> a precursor film model was implemented in which nominally dry regions of the substrate are assumed to be prewetted with an ultrathin uniform layer of liquid  $h_p \ll h_f$  identical in composition to the advancing liquid. The parameter  $h_p$  was chosen to be sufficiently small in

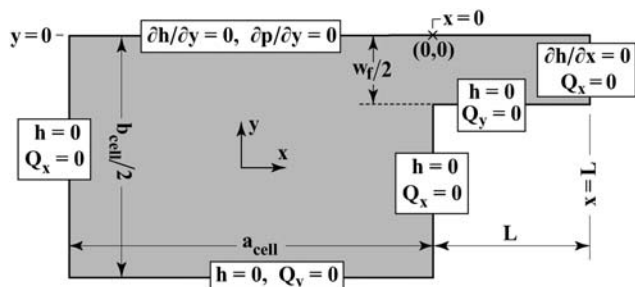


**Fig. 3** Computational domain and boundary conditions used for the hydrodynamic simulations. The stripe width  $w_f$  ranged from 0.5–2 mm; the stripe length length  $L$  ranged from 2–10 mm. The  $x$ -axis was chosen to coincide with the centerline of the wettable stripe. The origin  $(0, 0, 0)$  of the coordinate system is indicated by the location of the cross  $(x)$ .

order to avoid any noticeable effect on the computed droplet volumes.

The initial shape of the liquid on the supply cell was chosen to be

$$h(x, y, t = 0) = h_{\text{cell}} \left( 1 - \frac{4 \left( x - \frac{a_{\text{cell}}}{2} \right)^2}{a_{\text{cell}}^2} \right) \left( 1 - \frac{4y^2}{b_{\text{cell}}^2} \right) \quad (12)$$

encompassing a volume  $V_{\text{cell}} \sim (h_{\text{cell}} a_{\text{cell}} b_{\text{cell}})$ . The parameter  $h_{\text{cell}}$  was varied between 0.2–1.0 mm in order to adjust different values of  $V_{\text{cell}}$  ranging from 4–18  $\mu\text{l}$ .

## IV. Results and discussion

### A. Pre-dispensing – liquid filament formation

This next section describes the formation of a liquid filament of specified length spontaneously emanating from the supply cell by the combined action of capillary and hydrostatic pressure gradients,<sup>31</sup> as described by the augmented pressure  $\mathcal{P}_{\text{cell}}$ . In the experiments, the length of a liquid filament length was adjusted by activation of individual resistors  $R_i$ , which arrested the leading edge of the liquid at positions coinciding with the left edge of the resistors, namely  $x = 0, \Lambda, 2\Lambda$ , and  $3\Lambda$  or equivalently  $x = 0, 0.86, 1.72$  and  $2.58$  mm. Experimentally, the leading edge position was determined from optical microscopy by tracking the lowest-order dark interference fringe.

Fig. 4(a) shows an example of a computed center height profile of a liquid filament  $h_c(x) = h(x, y = 0)$  formed in this way. The corresponding increase in surface temperature  $T_s(x, y = 0) - T_{\text{ref}}$  and temperature gradient  $dT_s/dx(x, y = 0)$  for activation of resistor  $R_4$  with a power input of 12 mW is also shown for illustration. In these simulations, the filament width was set to  $w_f = 750$   $\mu\text{m}$  and the supply cell volume to  $V_{\text{cell}} = 14.5$   $\mu\text{l}$ . As discussed in Section III.A, the temperature profile is observed to decay within a distance  $\xi \approx 0.9$  mm. Therefore, the temperature of the surface of the supply cell as well as the liquid filament up to the location  $x \leq 1.5$  mm is essentially uniform.

The power  $P_i$  required to arrest the motion of the liquid filament to the left edge of resistor  $R_i$  is plotted in Fig. 4(b) as a function of  $V_{\text{cell}}$  for  $w_f = 2$  mm and  $i = 1 - 4$ . The simulation results (open symbols) are in very good agreement with the experimental data (filled symbols). In order to gauge the reproducibility of results from experiment, a series of 5 successive measurements of  $P_2$  was made for the case  $w_f = 1$  mm and  $V_{\text{cell}} = 12$   $\mu\text{l}$ ; these tests showed a variation in results of no more than a few percent.

The solid lines shown in Fig. 4 represent least-squared fits to the relation  $P_i = C_0 V_{\text{cell}}^2$ ; the corresponding fit parameters  $C_0$  are listed in Table 1. The holding power  $P_i$  necessary for maintaining a filament of a given length is observed to increase for positions situated closer to the supply inlet since the liquid film thickness is larger in this region. At the opposite end, the magnitude  $P_i$  is observed to asymptote to a constant value  $P_\infty$  for  $i \gg 1$  (*i.e.* for  $x_i \gg w_f$ ) since in this region the liquid film thickness becomes independent of  $x$ . The dependence of  $P_\infty$  on  $w_f$ , filament height  $h_f$  and microheater width  $w_R$  has been studied extensively in ref. [48].

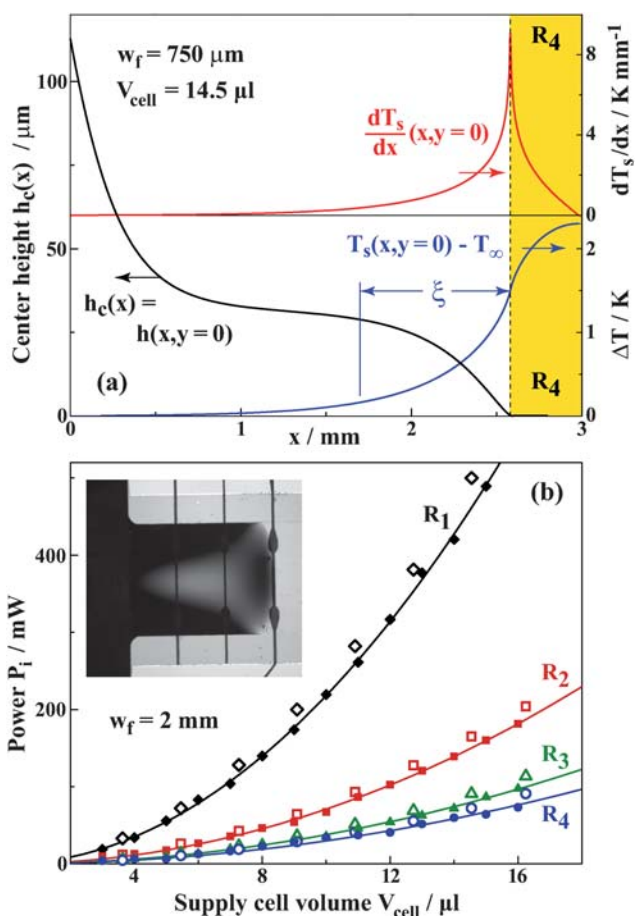


**Fig. 4** (a) Numerical simulations of the center height profile  $h_c(x) = h(x, y = 0)$ , the increase in surface temperature  $\Delta T = T_s(x, y = 0) - T_{ref}$ , and the corresponding temperature gradient  $dT_s/dx(x, y = 0)$  for the case  $w_f = 750 \mu\text{m}$ ,  $V_{\text{cell}} = 14.5 \mu\text{l}$  and activation of  $R_4$  with input power 12 mW. The position  $x = 0$  corresponds to the supply cell inlet; the rectangle (yellow-colored in online version) denotes the location of resistor  $R_4$  ( $x_4 = 2.98 \text{ mm}$ ). The parameter  $\xi$  indicates the lateral thermal decay length. (b) Comparison of the numerical simulations and experimental measurements for the power  $P_i$  applied to microheater  $R_i$  required to position the leading edge of the liquid filament at  $x_i = (i - 1)\Delta$  for  $w_f = 2 \text{ mm}$  and  $i = 1-4$ , i.e.  $x_i = 0, 0.86, 1.72$  and  $2.58 \text{ mm}$ . Solid symbols represent experimental values; open symbols represent hydrodynamic simulations. Inset: Optical micrograph of liquid filament on a 2 mm wide stripe arrested at leading edge position  $x = 2.58 \text{ mm}$  by activation of microheater  $R_4$ .

**1. Scaling analysis for low cell volumes.** In the limit of low  $V_{\text{cell}}$  and within the constraint of the lubrication approximation, it is possible to derive certain key scaling relations illustrating the operating characteristics of such a dispensing device. The next section focuses on three such relations involving the dependence of the filament height  $h_f$ , the holding power  $P_i$  required for affixing a given filament length, and the droplet volume dispensed  $V_{\text{drop}}$  as a function of increasing supply cell volume  $V_{\text{cell}}$ .

(i)  $h_f \sim V_{\text{cell}}$ . Under static conditions and in the absence of thermal gradients, the liquid configuration and shape is determined by the condition of constant pressure  $\mathcal{P}$ . Since both terms in Eq. (11) scale linearly with  $h$ , it follows that the filament pressure  $\mathcal{P}_f \sim h_f$ . An equivalent relation  $\mathcal{P}_{\text{cell}} \sim h_{\text{cell}}$  holds for

**Table 1** Numerical values of the fitting parameters  $C_i$  and  $\beta$  used in the various fit functions plotted in Figs. 4, 7 and 8. The parameter  $V_1 = 1.0 \mu\text{l}$  is introduced to make  $V_{\text{cell}}/V_1$  dimensionless, it is not a fitting parameter

Figure	Fitted function	Dataset	Parameter	Value	
Fig. 4(a)	Fitted function: $P_i = C_0 V_{\text{cell}}^2$	Dataset $C_0$ ( $10^{-4} \text{ mW}/\mu\text{l}^2$ )	$\blacklozenge$	$(21.8 \pm 0.1)$	
			$\blacksquare$	$(7.09 \pm 0.03)$	
			$\blacktriangle$	$(3.78 \pm 0.03)$	
			$\bullet$	$(2.98 \pm 0.05)$	
Fig. 7(a)	Fitted function: $P_{1,\text{min}} = C_4 V_{\text{cell}}^2$	Dataset $C_4$ ( $10^{-4} \text{ mW}/\mu\text{l}^2$ )	$\bullet$	$(8.346 \pm 0.071)$	
			$\blacksquare$	$(6.400 \pm 0.018)$	
			$\blacktriangle$	$(3.987 \pm 0.008)$	
			$\blacklozenge$	$(2.291 \pm 0.005)$	
Fig. 8(a)	Fitted function: $P_{1,\text{min}} = C_5 (V_{\text{cell}}/V_1)^\beta$ , $V_1 = 1 \mu\text{l}$	Dataset $C_5$ (nl)	$\beta$	$\Delta$	$(0.404 \pm 0.003)$
				$\circ$	$(1.244 \pm 0.046)$
				$\square$	$(3.057 \pm 0.128)$
				$\diamond$	$(15.03 \pm 0.37)$
					$(0.987 \pm 0.010)$

liquid on the supply cell. Accordingly, it holds that  $\mathcal{P}_f = \mathcal{P}_{\text{cell}}$ . Additionally, the cell volume is proportional to the cell height  $V_{\text{cell}} \sim a_{\text{cell}} b_{\text{cell}} h_{\text{cell}}$ . Consequently,  $V_{\text{cell}} \sim h_{\text{cell}} \sim \mathcal{P}_{\text{cell}}$  and thus  $h_f \sim V_{\text{cell}}$ .

(ii)  $P_i \sim V_{\text{cell}}^2$ . A stationary filament on a liquid stripe represents a steady-state solution of Eq. (8), i.e.  $\partial h/\partial t = 0$  for which there is neither flow in the  $x$  or  $y$  directions. The two contributions in  $Q_x$  must therefore balance. Since the first term scales as  $h_f^2 \tau$  while the second term scales as  $h_f^4$ , it is evident that the shear stress  $\tau \sim h_f^2$ . For regions sufficiently far from an activated microheater where  $\tau(x)$  has decayed to a sufficiently small value, the system is characterized by a constant pressure, i.e.  $\mathcal{P}_{\text{cell}} = \mathcal{P}_f \sim h_f$ . The relation derived above,  $h_f \sim V_{\text{cell}}$ , therefore serves as a matching condition. As noted in the previous section, the increase in surface temperature and hence the increase in  $\tau$  is linearly proportional to the input power,  $P_i \propto \tau$ . Combining these relations yields that  $P_i \sim h_f^2 \sim V_{\text{cell}}^2$ , which is found to reproduce the experimental curves in Fig. 4(b) rather well.

(iii)  $V_{\text{drop}} \sim V_{\text{cell}}$ . From strictly geometric considerations, it is the case that  $V_{\text{drop}} \sim h_f w_f L_f$ , where  $L_f$  is chosen by the operator of the device. According to (i),  $h_f \sim V_{\text{cell}}$ ; therefore the droplet volume scales is expected to scale proportionally with the supply cell volume  $V_{\text{drop}} \sim V_{\text{cell}}$ .

**2. Dynamics of filament formation.** Liquid filament formation resulting from passive spreading of liquid from the supply cell due to hydrostatic and capillary pressure gradients is a relatively slow process for the low supply volumes examined in this study. Thermally assisted flow from the supply cell, however, substantially accelerates formation. For this purpose, a curved heating element  $R_0$  was fabricated beneath the supply cell as sketched in Fig. 1(a). Fig. 5(a) shows results for the time required,  $t_{2-4}$ , for a liquid filament of width  $750 \mu\text{m}$  initially held at the left edge of resistor  $R_2$  ( $x = \Delta$ ) to flow to the left edge of  $R_4$  ( $x = 3\Delta$ ) while  $R_5$  was activated with  $P_5 = 14 \text{ mW}$ . The time intervals,  $t_{2-4}$ , were recorded as a function of  $V_{\text{cell}}$  either with (solid diamonds) or without (solid squares) activation of resistor  $R_0$  powered at  $P_0 = 262 \text{ mW}$ . The stripe was prewet with

a precursor layer of approximate thickness 80 nm in order to facilitate comparison with numerical calculations (open symbols).

The formation time  $t_{2-4}$  decreases with increasing supply cell volume because the higher supply pressure and resulting larger film thickness both accelerate the flow.<sup>31</sup> Activation of  $R_0$  significantly reduced the time needed for liquid filament generation, especially at low supply cell volumes. Since the distance between  $R_0$  and the stripe inlet exceeded the decay length  $\xi \approx 0.9$  mm, the thermocapillary stresses did not increase the flow rate directly. Rather, the acceleration effect is due to an increase in the augmented pressure near the inlet region,  $\mathcal{P}_{\text{inlet}} = \mathcal{P}(x = 0, y = 0) \geq \mathcal{P}_{\text{cell}}(P_0 = 0)$ . The influence of  $R_0$  in expediting liquid filament generation is diminished for larger supply cell volumes, since for larger values of  $V_{\text{cell}}$  the relative increase in  $\mathcal{P}_{\text{inlet}}$  is smaller.

In the remainder of this section, a scaling relation between  $t_{2-4}$  and the supply cell volume  $V_{\text{cell}}$  is derived to compare with the experimental results in Fig. 5(a). Since for the duration of  $t_{2-4}$  the distance between the spreading liquid filament and the activated microheater  $R_5$  exceeds the thermal decay length  $\xi$ , it is possible to revert simply to a description of isothermal spreading due to gradients in capillary pressure, as previously derived.<sup>31</sup> According to Eq. (9), the height averaged velocity  $\langle u \rangle$  scales as  $h^2 \partial \mathcal{P} / \partial x \sim h_f^3$  in regions where the magnitude of the thermocapillary stress  $\tau$  is negligible. Consequently, it is expected that

$$t_{2-4}(P_0 = 0) \sim \frac{(x_4 - x_2)}{\langle u \rangle} \sim h_f^{-3} \sim \mathcal{P}_{\text{cell}}^{-3} \sim V_{\text{cell}}^{-3} \quad (13)$$

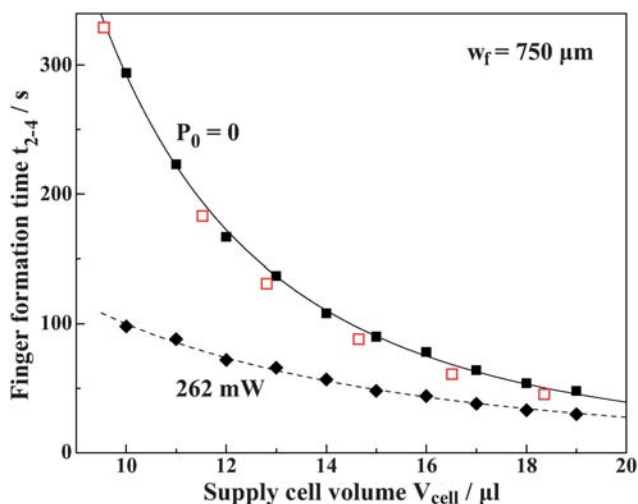


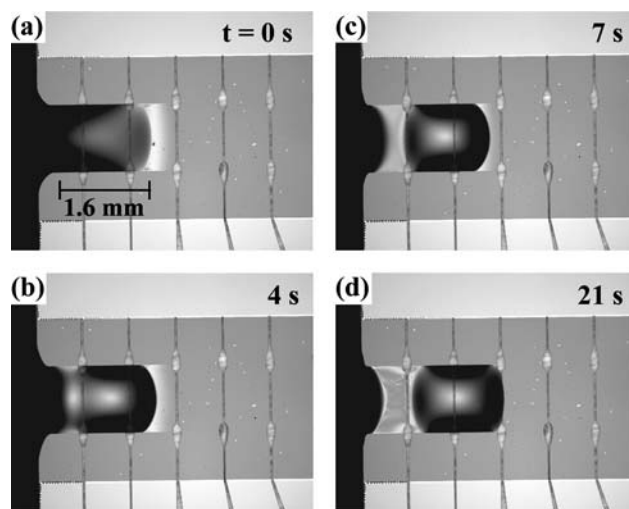
**Fig. 5** Experimental measurements of the time interval required,  $t_{2-4}$ , for a liquid filament of width  $750 \mu\text{m}$  initially stationed at the left edge of resistor  $R_2$  to flow to the left edge of  $R_4$  with activation of  $R_5$  at  $P_5 = 14$  mW. Measurements were taken with (solid diamonds) and without (solid squares) thermal assist from  $R_0$  with  $P_0 = 262$  mW. Open symbols represent results of hydrodynamic simulations for the flow process. The solid line corresponds to least-squared fits of the form  $t_{2-4} = C_1(V_{\text{cell}}/V_1)^{\beta_1}$ , where  $C_1 = (2.3 \pm 0.2) \cdot 10^5$  s and  $\beta_1 = (-2.896 \pm 0.036)$ . The constant  $V_1 = 1.0 \mu\text{l}$  only serves to non-dimensionalize  $V_{\text{cell}}/V_1$ . The dashed line is only a guide to the eye.

The exponent  $\beta_1 = (-2.896 \pm 0.036)$  obtained from a least-squared fit of the data (solid squares) in Fig. 5(a) is close to the exponent  $-3$  from this scaling prediction.

## B. Droplet dispensing

Once a filament of a given length is generated, it can then be divided into parcels of liquid by activation of multiple resistors. The heat generated from these thin film heaters expels liquid from the warmer regions to assist the formation of discrete droplets. In what follows, experiments were restricted to the generation of a single droplet near the stripe inlet for liquid filaments of width  $w_f = 0.5, 0.75, 1$  or  $2$  mm. In all cases, the filament length was adjusted to  $L_f \approx 1.6$  mm by activation of resistor  $R_4$ . A typical splitting sequence is shown in Fig. 6 for a  $1$  mm wide liquid ribbon. The first frame shows the filament just prior to activation of  $R_1$ . In subsequent frames, the furrow which appears above  $R_1$  progressively deepens. After approximately  $7$  s a droplet becomes separated from the supply cell; the connecting film, which undergoes continuous thinning, was monitored by the formation and movement of optical interference fringes in this region; Eq. (8) indicates that the droplet formation time is inversely proportional to the liquid viscosity  $\mu$ . At sufficiently high powers  $P_1$ , the thinning of this connecting film proceeds asymptotically<sup>48</sup> as  $h = A/(t - t_0)$ , where the constant  $A$  is proportional to  $P_1^{-1}$ .

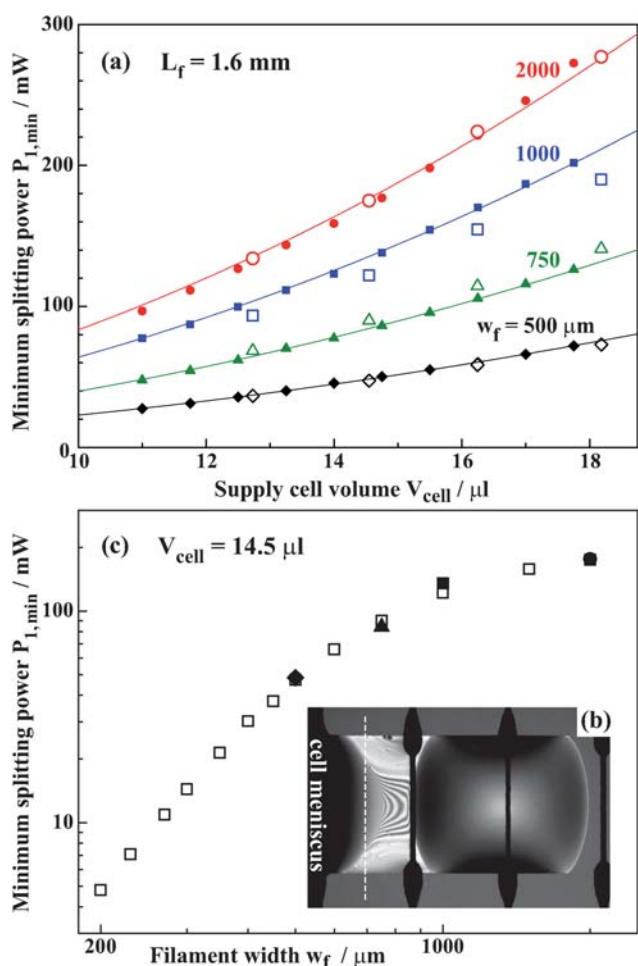
The minimum power  $P_{1,\text{min}}$  required to suppress continued flow from the supply cell into a detached droplet using the thermocapillary stress generated by  $R_1$  as a function of increasing  $V_{\text{cell}}$  is plotted in Fig. 7(a). The solid symbols represent experimental results for stripe widths  $w_f = 0.5, 0.75, 1$  and  $2$  mm. The open symbols represent data obtained from the hydrodynamic simulations. There is good agreement between the experimental and computational results. The solid lines shown represent least-squared fits to the relation  $P_{1,\text{min}} \sim V_{\text{cell}}^2$ , which appears to be an excellent approximation to both the experimental and numerical results. Deviations from this scaling, which are approximately 10%, are likely due to variations in the precise location of  $R_1$  with



**Fig. 6** (a–d) Optical micrographs illustrating the scission of a liquid filament  $1$  mm in width by activation of resistor  $R_1$ .

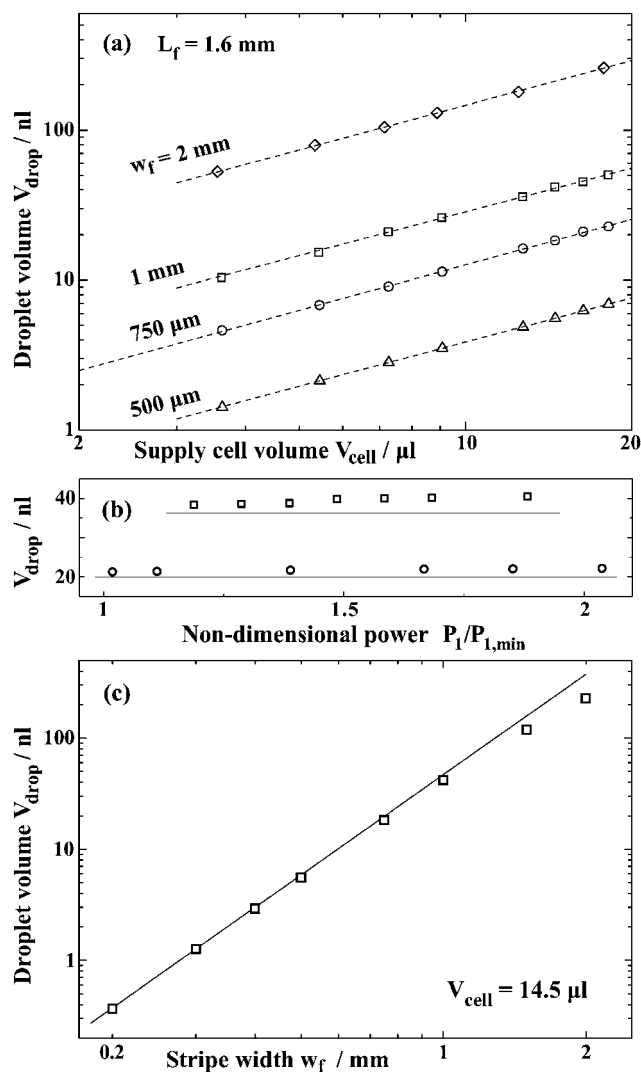
respect to the cell inlet, which ultimately affect the actual value of  $P_{1,\min}$ . In the vicinity of the inlet, the liquid undergoes a strong variation in height. As a consequence, any photolithographic misalignment on the order of  $\Delta x = 20 \mu\text{m}$  during device fabrication can induce a change in  $P_{1,\min}$  on the order of 10%.

Fig. 7(b) shows an optical micrograph of a liquid filament on a 1 mm wide stripe for the case of insufficient power  $P_1 < P_{1,\min}$ . The optical interference fringes indicate the existence of a substantial liquid bridge in between the supply cell meniscus and the drop. Liquid is continually pumped into the droplet through this bridge thereby increasing the droplet volume. Given sufficient time and in the absence of evaporation, this process



**Fig. 7** (a) Minimum heating power  $P_{1,\min}$  required for droplet detachment by activation of  $R_1$  for filament widths  $w_f = 0.5, 0.75, 1$  and  $2 \text{ mm}$  as a function of increasing supply cell volume. Solid symbols represent results of experimental measurements; open symbols denote results of hydrodynamic simulations. The solid lines represent least-squared fits to the function  $P_{1,\min} \sim V_{\text{cell}}^2$ ; the corresponding fitting parameters are listed in Table 1. (b) Optical micrograph of liquid filament on a 1 mm wide stripe for  $P_1 < P_{1,\min}$ . The interference fringes designate the presence of a substantial film connecting the meniscus near the supply cell to the droplet. The dashed line denotes the center of microheater  $R_1$  ( $x = 400 \mu\text{m}$ ). (c) Minimum splitting power  $P_{1,\min}$  required for detachment of a droplet as a function of filament width  $w_f$  for  $V_{\text{cell}} = 14.5 \mu\text{l}$ . Open symbols denote results of hydrodynamic simulations; solid symbols represent values obtained from the least squared fits in (a) for  $V_{\text{cell}} = 14.5 \mu\text{l}$ .

gradually leads to a thickening of the liquid bridge and re-coalescence of the drop with the liquid in the supply cell. This non-monotonic behavior of the liquid film thickness above microheater  $R_1$  is a consequence of the asymmetry and rapid variation of the height profile near the inlet. It does not occur in the symmetric splitting of long liquid filaments, where the liquid filament thickness above the resistor decreases monotonically.<sup>48</sup> In geometric terms, detachment of a droplet requires a sufficiently high temperature gradient such that the leading edge of the cell meniscus recedes to the left of the center of  $R_1$ . For the device layouts used in this study, this situation corresponds to



**Fig. 8** (a) Numerical solutions for the droplet volume  $V_{\text{drop}}$  formed by detachment, as shown in Fig. 6, as a function of the volume of liquid on the supply cell  $V_{\text{cell}}$ . The dashed lines correspond to least-squared fits to the relation  $V_{\text{drop}} \sim V_{\text{cell}}^3$ ; the corresponding fitting parameters are listed in Table 1. (b) Numerical solutions for the droplet volume  $V_{\text{drop}}$  as a function of the power  $P_1$  applied to microheater  $R_1$  for (i)  $w_f = 750 \mu\text{m}$  and  $V_{\text{cell}} = 18 \mu\text{l}$  (circles,  $\circ$ ) and (ii)  $w_f = 1 \text{ mm}$  and  $V_{\text{cell}} = 14.5 \mu\text{l}$  (squares,  $\square$ ). The horizontal solid lines serve only as a guide to the eye. (c) Numerical solutions for the droplet volume  $V_{\text{drop}}$  as a function of stripe width  $w_f$  for  $V_{\text{cell}} = 14.5 \mu\text{l}$ . The solid line corresponds to the power law relation  $V_{\text{drop}} = C_6 w_f^3$  with  $C_6 = 4.69 \times 10^{-2}$ .

a leading edge position  $x_{\text{apex}} \leq 400 \mu\text{m}$ , as indicated by the white dashed line in Fig. 7(b). The same criterion for determination of  $P_{1,\text{min}}$  was used for the experiment and hydrodynamic simulations.

Fig. 7(c) illustrates the dependence of  $P_{1,\text{min}}$  on the filament width  $w_f$  for  $V_{\text{cell}} = 14.54 \mu\text{l}$ . For small  $w_f$ ,  $P_{1,\text{min}}$  varies strongly with  $w_f$  but progressively less so with increasing values of  $w_f$ . In principle, the power  $P_{1,\text{min}}$  (per unit length of the microheaters in the  $y$ -direction) will saturate for large widths  $w_f \gg l_c$  at a value  $P_{\text{sat}}$ . Here,  $l_c = \sqrt{\gamma/(\rho g)} \approx 1.5 \text{ mm}$  is the capillary length scale. The parameter  $P_{\text{sat}}$  corresponds to the minimum power (per unit length) required to split a thin liquid film of infinite extent by activation of  $R_1$  and  $R_4$ . In practice, however, the cell width and the resistor length provide upper limits for  $w_f$  and the saturation regime is therefore never attained.

Fig. 8 shows results of numerical simulations for the behavior of the dispensed volumes  $V_{\text{drop}}$  as a function of various operating or design parameters. Fig. 8(a) indicates the behavior of  $V_{\text{drop}}$  with increasing values of the supply cell volume. Since  $L_f$  was chosen to be constant, it is expected that the droplet volume  $V_{\text{drop}} \sim V_{\text{cell}}$ , as discussed previously in Section IV.A.1(iii). The dashed lines represent fits to the power law  $V_{\text{drop}} \sim V_{\text{cell}}^\beta$ , where  $\beta$  ranges between 0.96 and 1 (see Table 1). The simulations reproduce the expected scaling quite well. Fig. 8(b) shows the results for  $V_{\text{drop}}$  with increasing power  $P_1$ . The droplet volume could in principle depend on  $P_1$  because the microheater  $R_1$  is located close to the cell inlet where the height profile varies rapidly. However, as can be seen from Fig. 8(b),  $V_{\text{drop}}$  depends only weakly on the ratio  $P_1/P_{1,\text{min}}$ , an advantageous feature for device applications.

Fig. 8(c) illustrates the dependence of  $V_{\text{drop}}$  on  $w_f$  for  $V_{\text{cell}} = 14.5 \mu\text{l}$ . For  $w_f < l_c$  the hydrostatic contribution to the augmented pressure  $\mathcal{P}$  in Eq. (11) is negligible. Under static conditions, then, the constraint that the pressure be a constant throughout the fluid requires  $\mathcal{P}_{\text{cell}} = \mathcal{P}_f \sim \gamma h_f/w_f^2 = \text{const}$ , or equivalently,  $h_f \sim w_f^2$ . The droplet volume  $V_{\text{drop}} \sim h_f w_f L_f$  is therefore expected to

scale as  $w_f^3 L_f$ . The solid line in Fig. 8(c) corresponds to the power law relation  $V_{\text{drop}} = C_6 w_f^3$ , which is found to agree well with the numerical data shown for  $w_f \leq 1 \text{ mm}$ .

## V. Summary

This work describes the advantageous design and operating principles for a planar digital nanoliter dispensing system based on thermocapillary actuation of liquids on chemically patterned surfaces. Electronic activation of a linear array of embedded microheaters is used to vary the surface tension of an overlying liquid film. Two distinct liquid handling processes are investigated. Liquid residing on a planar rectangular supply cell is first made to flow spontaneously (by capillary and hydrostatic forces) onto the surface of a slender stripe defined against a non-wetting background. The monolayer treatment used to define non-wetting regions effectively prevents migration of liquid outside the wettable regions. The length of the liquid filament formed in this way is electronically controlled by activation of a resistive heating element. Activation of the selected microheater generates a reverse thermocapillary stress, which counteracts the spontaneous spreading process and arrests the leading edge of the filament at a chosen location. Once a filament of a given length is formed, additional microheaters can be activated to induce thermocapillary splitting at one or more locations. The liquid film in the vicinity of the activated microheaters heats up and is therefore driven away by thermocapillary stresses, leading to controlled thinning at predefined positions. The results of hydrodynamic and heat transfer simulations within the lubrication approximation for both stages of liquid drop formation are found to be in excellent agreement with experimental measurements. Scaling relations are derived for the characteristic thickness of liquid filaments, the holding power required to generate a filament of given length, and the minimum splitting power required to dispense a single droplet as a function of the liquid supply volume and geometric device parameters. The capability

**Table 2** Operating parameters of different dispensing methods. The symbols  $\Delta t$  and  $U$  denote the dispensing time and actuation speed, respectively

Method	Liquid	Voltage (V)	$V_{\text{drop}}$ (nl)	$\Delta t$ (s)	$U$ (mm/s)	Ref.
Electrowetting	water	$\geq 15$	460	–	–	[55]
	water	$\geq 25$	50–900	–	$\leq 250$	[21]
	water	55	50–2000	$\geq 0.5$	–	[23]
	water	15–100	$\geq 3$	–	$\leq 300$	[6]
Dielectrophoresis	water	120	$\geq 0.003$	–	$\sim 1.8$	[56]
	water	250–400	–	–	$\leq 18$	[7]
	water	700	$\geq 6 \text{ nl}$	$< 0.1$	–	[8]
	water	250	$> 0.5$	$\sim 0.1$	$\sim 50$	[57]
	water, dodecane	200–600	500–1000	–	$\leq 2$	[58]
Thermocapillary actuation	PDMS, hexadecane	200–1300	50–200	–	$\leq 4$	[59]
	PDMS	1–6	3–300	20–300	–	this work
	various	5–6	20–200	–	0.008–0.3	[32]
	various	15–25	10–100	–	0.1	[4]
SAW	PDMS	–	$\sim 1200$	–	$\sim 0.4$	[60]
	water	RF	0.02–100	–	$\leq 12$	[9]
Pin transfer	glycerol, TEG <sup>a</sup>	–	$\leq 40 \cdot 10^{-9}$	–	–	[19]
	water	–	$\sim 10 \text{ nl}$	$\sim 1$	–	[61]
Inkjet deposition	various	3–30	4–65	$\geq 0.001$	$\leq 3000$	[62]
	–	–	60–800	–	$\leq 5500$	[63]
	various	–	$\geq 0.01$	$\geq 0.0001$	$\leq 6000$	[64]

<sup>a</sup> TEG is an abbreviation for tetra(ethylene glycol)

to dispense nanoliter volumes onto a 2D substrate extends the functionality of microfluidic devices based on thermocapillary actuation, previously shown effective in routing and mixing liquid samples on glass or silicon substrates. Such a dispensing device can also be easily integrated with alternative microfluidic devices utilizing free surface flows.

## Appendix

Tab. 2 compares performance parameters of different dispensing methods. The authors wish to stress that the quoted information refers to the specific implementations in the listed publications and may not reflect fundamental requirements or limitations.

## Acknowledgements

This research was financed by the National Science Foundation through grants CTS 0649474 and CBET 0701324 (SMT). AAD gratefully acknowledges that this research is supported partially by the Dutch Technology Foundation STW, applied science division of NWO and the Technology Program of the Ministry of Economic Affairs.

## References

- 1 A. A. Darhuber and S. M. Troian, *Annu. Rev. Fluid Mech.*, 2005, **37**, 425.
- 2 E. Stemme and G. Stemme, *Sens. Actuators, A*, 1993, **39**, 159.
- 3 A. Manz, C. S. Effenhauser, N. Burggraf, D. J. Harrison, K. Seiler and K. Flurri, *J. Microelectromech. Syst.*, 1994, **4**, 257.
- 4 T. S. Sammarco and M. A. Burns, *AIChE J.*, 1999, **80**, 350.
- 5 J. Lee and C. J. Kim, *J. Microelectromech. Syst.*, 2000, **9**, 171.
- 6 M. G. Pollack, R. B. Fair and A. D. Shenderov, *Appl. Phys. Lett.*, 2000, **77**, 1725.
- 7 J. S. Batchelder, *Rev. Sci. Instrum.*, 1982, **54**, 300.
- 8 T. B. Jones, M. Gunji, M. Washizu and M. J. Feldman, *J. Appl. Phys.*, 2001, **89**, 1441.
- 9 C. J. Strobl, Z. v. Guttenberg and A. Wixforth, *IEEE Trans. Ultrason. Ferroelectr. Freq. Control*, 2004, **51**, 1432.
- 10 A. A. Darhuber, J. P. Valentino, J. M. Davis, S. M. Troian and S. Wagner, *Appl. Phys. Lett.*, 2003, **82**, 657.
- 11 B. Nguon and M. Jouaneh, *Int. J. Adv. Manuf. Technol.*, 2004, **24**, 251.
- 12 D. B. Bogy, *Annu. Rev. Fluid Mech.*, 1979, **11**, 207.
- 13 H. P. Le, *J. Imag. Sci. Technol.*, 1998, **42**, 49.
- 14 Q. Xu and O. A. Basaran, *Phys. Fluids*, 2007, **19**, 102111.
- 15 M. J. Heller, *Annu. Rev. Biomed. Eng.*, 2002, **4**, 129.
- 16 J. Zeng, M. Deshpande, H.-C. Kan, and J. R. Gilbert, in *Micro Total Analysis Systems 2001*, p. 143, Kluwer Academic, Dordrecht, 2001.
- 17 M. Jaschke and H.-J. Butt, *Langmuir*, 1995, **11**, 1061.
- 18 R. D. Piner, J. Zhu, F. Xu, S. Hong and C. A. Mirkin, *Science*, 1999, **283**, 661.
- 19 A. Meister, M. Liley, J. Brugger, R. Pugin and H. Heinzelmann, *Appl. Phys. Lett.*, 2004, **85**, 6260.
- 20 A. Fang, E. Dujardin and T. Ondarcuhu, *Nanoletters*, 2006, **6**, 2368.
- 21 S. K. Cho, H. Moon and C. J. Kim, *J. Microelectromech. Syst.*, 2003, **12**, 70.
- 22 M. G. Pollack, A. D. Shenderov and R. B. Fair, *Lab Chip*, 2002, **2**, 96.
- 23 H. Ren, R. B. Fair and M. G. Pollack, *Sens. Actuators, B*, 2004, **98**, 319.
- 24 U. C. Yi and C. J. Kim, *Sens. Actuators, A*, 2004, **114**, 347.
- 25 F. Mugele and J.-C. Baret, *J. Phys.: Condens. Matter*, 2005, **17**, R705.
- 26 P. R. C. Gascoyne, J. V. Vykoukal, J. A. Schwartz, T. J. Anderson, D. M. Vykoukal, K. W. Current, C. McConaghy, F. F. Becker and C. Andrews, *Lab Chip*, 2004, **4**, 299.
- 27 A. A. Darhuber, S. M. Troian, J. M. Davis, S. M. Miller and S. Wagner, *J. Appl. Phys.*, 2000, **88**, 5119.
- 28 Lord Rayleigh, *Proc. R. Soc. London*, 1879, **29**, 71; Lord Rayleigh, *Phil. Mag.*, 1892, **34**, 145.
- 29 S. Tomotika, *Proc. R. Soc. London, Ser. A*, 1935, **150**, 322.
- 30 S. H. Davis, *J. Fluid Mech.*, 1980, **98**, 225.
- 31 A. A. Darhuber, W. W. Reisner and S. M. Troian, *Phys. Rev. E: Stat., Nonlinear, Soft Matter Phys.*, 2001, **64**, 0316031.
- 32 A. A. Darhuber, J. P. Valentino, S. M. Troian and S. Wagner, *J. Microelectromech. Syst.*, 2003, **12**, 873.
- 33 A. A. Darhuber, J. M. Davis, S. M. Troian and W. W. Reisner, *Phys. Fluids*, 2003, **15**, 1295.
- 34 J.-Z. Chen, A. A. Darhuber, S. M. Troian and S. Wagner, *Lab Chip*, 2004, **4**, 473.
- 35 J. P. Valentino, S. M. Troian and S. Wagner, *Appl. Phys. Lett.*, 2005, **86**, 1841011.
- 36 A. A. Darhuber, J. Z. Chen, J. M. Davis and S. M. Troian, *Philos. Trans. R. Soc. London, Ser. A*, 2004, **362**, 1037.
- 37 K. T. Kotz, Y. Gu and G. W. Faris, *J. Am. Chem. Soc.*, 2005, **127**, 5736–5737.
- 38 C. N. Baroud, J.-P. Delville, F. Gallaire and R. Wunnenburger, *Phys. Rev. E: Stat., Nonlinear, Soft Matter Phys.*, 2007, **75**, 046302.
- 39 A. S. Basu and Y. B. Gianchandani, *J. Micromech. Microeng.*, 2008, **18**, 115031.
- 40 Y.-F. Yap, S.-H. Tan, N.-T. Nguyen, S. M. Sohel Murshed, T.-N. Wong and L. Yobas, *J. Phys. D: Appl. Phys.*, 2009, **42**, 065503.
- 41 A. W. Adamson, *Physical Chemistry of Surfaces*, Wiley (New York, 1990).
- 42 B. Singh and N. A. Surplice, *Thin Solid Films*, 1972, **10**, 243.
- 43 J. Caballero, G. Kremer and L. A. Moraga, *Thin Solid Films*, 1984, **117**, 1.
- 44 G. T. Dyos and T. Farrell (eds.), *Electrical Resistivity Handbook*, Peter Peregrinus (Herts, 1992).
- 45 B. Sauer and G. T. Dee, *Macromolecules*, 1991, **24**, 2124.
- 46 E. G. Rochow, *An Introduction to the Chemistry of the Silicones*, John Wiley & Sons, New York, 1951.
- 47 A. A. Darhuber, S. M. Troian and S. Wagner, *J. Appl. Phys.*, 2002, **91**, 5686.
- 48 A. A. Darhuber and S. M. Troian, *J. Appl. Phys.*, submitted.
- 49 The Reynolds number  $Re = \rho h_f U / \mu \approx 0.0005$  is usually very small, where  $U \approx 100 \mu\text{m/s}$  is a typical velocity and  $h_f = 100 \mu\text{m}$  a typical filament height.
- 50 A. Oron, S. H. Davis and S. G. Bankoff, *Rev. Mod. Phys.*, 1997, **69**, 931.
- 51 G. Friz, *Z. Angew. Phys.*, 1965, **19**, 374.
- 52 E. B. Dussan and S. H. Davis, *J. Fluid Mech.*, 1974, **65**, 71.
- 53 L. H. Tanner, *J. Phys. D: Appl. Phys.*, 1979, **12**, 1473.
- 54 P. M. de Gennes, *Rev. Mod. Phys.*, 1985, **57**, 827.
- 55 H. Moon, S. K. Cho, R. L. Garrell and C.-J. Kim, *J. Appl. Phys.*, 2002, **92**, 4080.
- 56 J. A. Schwartz, J. V. Vykoukal and P. R. C. Gascoyne, *Lab Chip*, 2004, **4**, 11.
- 57 M. R. King, O. A. Lomakin, R. Ahmed and T. B. Jones, *J. Appl. Phys.*, 2005, **97**, 054902.
- 58 O. D. Velev, B. G. Prevo and K. H. Bhatt, *Nature*, 2003, **426**, 515.
- 59 S.-K. Fan, T.-H. Hsieh and D.-Y. Lin, *Lab Chip*, 2009, **9**, 1236.
- 60 N.-T. Nguyen and X. Huang, *Jpn. J. Appl. Phys.*, 2005, **44**, 1139.
- 61 P. E. Sheehan, R. L. Edelstein, C. R. Tamanaha and L. J. Whitman, *Biosens. Bioelectron.*, 2003, **18**, 1455.
- 62 J. Sun, J. Hao Ng, Y. H. Fuh, Y. S. Wong, H. T. Loh and Q. Xu, *Microsyst. Technol.*, 2009, **15**, 1437.
- 63 B. de Heij, C. Steinert, H. Sandmaier and R. Zengerle, *Sens. Actuators, A*, 2003, **103**, 88.
- 64 M. McDonald, *Proc. 19th Int. Conf. on Digital Printing Technologies*, New Orleans, 2003, p. 555.